Ocean Engineering 285 (2023) 115256

Contents lists available at ScienceDirect

Ocean Engineering

journal homepage: www.elsevier.com/locate/oceaneng

Generation of incident wave in two-phase flow simulation based on field decomposition

Tietao Lao, Zhaobin Li, Zhiying Wang, Zhan Wang, Zixuan Yang *

Institute of Mechanics, Chinese Academy of Sciences, Beijing, 100190, PR China
School of Engineering Science, University of Chinese Academy of Sciences, Beijing, 100049, PR China

ARTICLE INFO

Keywords:
Velocity decomposition
Wave generation
Two-phase flow

ABSTRACT

Field decomposition is an effective strategy for reducing numerical dissipation and dispersion. This strategy was employed by Li et al. (2021) to generate incident waves in two-phase flow simulations. This study attempts to improve previous methods in two ways. First, the density gradient in the additional source term, i.e. a delta function at the interface, is explicitly discretised. Although the explicit calculation simplifies the implementation, an additional pressure translation correction method is proposed to ensure numerical stability and accuracy. Second, the coupled level-set and volume-of-fluid method is used for interface capture. The calculation of the additional source term is more precise using the level-set function. The two proposed improvements result in a second-order spatial accuracy for the wave amplitude. A test on wave propagation over a flat bottom shows that the proposed method provides more accurate predictions of the wave amplitude compared with the previous method. In other test cases, including wave propagation over two-dimensional breakwater and three-dimensional shoal, the simulation results show good agreement with the experimental data.

1. Introduction

In computational fluid dynamics (CFD) studies of wave–structure interactions, generating accurate incident waves is a key technique. Several wave generation approaches have been developed, including internal wave generation, static-boundary wave generation, and moving-boundary wave generation (Higuera et al., 2015). Despite the success of the wave generation approaches, the numerical simulation of water wave propagation is challenging, because numerical dissipation and dispersion result in non-physical wave attenuation and phase shift (Paulsen et al., 2014; Tao, 2020). Regardless of the selected wave generation method, the waves undergo non-physical attenuation and phase shift owing to the numerical dissipation and dispersion associated with the Navier–Stokes equation solver (Paulsen et al., 2014; Tao, 2020). Although such numerical errors can be reduced by refining the mesh, reducing the time step, or adopting a higher-order accuracy scheme, these are accompanied by increased computational costs. When the wave motion is described by a potential theory, it can be solved either analytically or numerically through a high-order accuracy scheme to avoid numerical dissipation and dispersion. The potential-flow method can be also used to solve wave–structure interaction problems, and results show good agreement with experiments and numerical simulations based on viscous-flow solvers (Islam et al., 2019; Mohapatra et al., 2020, 2022).

The velocity decomposition strategy, which combines the advantages of different flow solvers, has been used in many CFD applications, such as phase change (Lu et al., 2023), turbulent wake (Edmund et al., 2013; Mittal et al., 2017), interactions between vortex tubes and free surface (Dommermuth, 1993), and the coupled motion of viscous fluid and elastic material interface (Beale and Layton, 2009). When the velocity decomposition strategy is used for wave generation, the velocity field can be decomposed into an incident part and a complementary part. The incident part can be obtained using a high-accuracy potential flow solver (Choi et al., 2023). Thus, the incident wave propagation is not influenced by the numerical errors corresponding to the Navier–Stokes equation solver. The complementary part can be solved using the Navier–Stokes equation solver by adding some derived source terms. Using this velocity decomposition strategy, Ferrant et al. (2003) studied the interaction between a regular wave and square body based on a single-phase simulation. This method was subsequently called the Spectral Wave Explicit Navier–Stokes Equation (SWENSE) by Luquet

* Corresponding author at: Institute of Mechanics, Chinese Academy of Sciences, Beijing, 100190, PR China.
E-mail address: yangzx@imech.ac.cn (Z. Yang).

https://doi.org/10.1016/j.oceaneng.2023.115256
Received 19 April 2023; Received in revised form 10 June 2023; Accepted 24 June 2023
Available online 11 July 2023

et al. (2003). Compared with the pure Navier–Stokes equation solver, the SWENSE method reduced the computational time by approximately 50% while achieving the same accuracy in the prediction of wave amplitude (Luquet et al., 2007).

Vukčević et al. (2016a,b) extended the SWENSE method to two-phase flow simulations. They applied the decomposition strategy to the velocity field; however, the pressure field remained undecomposed. In their algorithm, a phase-field method coupled with the level-set (LS) method was used for interface capture, with the density smeared in two or three grid points. Later, Li et al. (2019, 2021) pointed out that applying pressure-field decomposition was crucial to satisfying the two basic requirements of the governing equations of the complementary part. These are the (1) degeneration to an Euler equation when the complementary flow is trivial and (2) degeneration to the Navier–Stokes equation when there are no incident waves. They derived the conservative form of the momentum equation of the complementary velocity, in which two additional terms appeared. One was derived from the non-linear term of the Navier–Stokes equation, while the other was associated with the pressure of the incident flow. The volume-of-fluid (VOF) method (Hirt and Nichols, 1981) was used by Li et al. (2019, 2021) to capture the interface. To keep the interface sharp, they treated the additional term with the pressure similar to the surface tension using a ghost-fluid (GF) method (Liu et al., 2000). They further compared the performance of the SWENSE method with that of the internal wave generation and static-boundary wave generation methods for generating incident waves. They found that the number of grid points required by the SWENSE method was only 25% of that required by the other two methods to achieve the same wave amplitude accuracy.

Previous studies show that the performance of the SWENSE method relies on the interface calculation method. The summary of different interface calculation methods can be found in Mirjalili et al. (2017, 2019). Generally speaking, a sharp-interface treatment is usually preferable to obtain more accurate results. The VOF method can be regarded as a sharp-interface method. Specifically, the transition of density in the VOF method occurs only in one layer of grid cells between two phases. Li et al. (2019, 2021) adopted an algebraic VOF method by using the compression velocity for keeping interface sharp, while advanced and accurate geometric VOF method was developed by Roenby et al. (2016), Nguyen and Park (2016), Pathak et al. (2023), which has been successfully applied for simulating waves (Nguyen and Park, 2018). In the LS method, the density is usually determined by a mollified Heaviside function of the signed distance of each grid point to the interface. If the transition thickness of the mollified Heaviside function is smaller than one grid width, the LE method is regarded as a sharp-interface method.

In this study, we extended the SWENSE method to a coupled LS and VOF (CLSVOF) interface-capturing framework (Sussman and Puckett, 2000). Using the LS function, the location of the interface can be identified more accurately for the more precise calculation of the incident pressure at the interface. The LS method has been used to simulate non-breaking and breaking waves with good results (Bihs et al., 2016; Iafrati, 2009). The LS function is not a conserved quantity, and as such a reinitialisation algorithm needs to be adopted to ensure the mass conservation. In our method, the VOF method is coupled to reconstruct the interface to avoid non-physical loss of fluid volume. The LS function is updated through a direct calculation of the distance of a grid point to the reconstructed interface. Thus, the reinitialisation algorithm is no longer needed. To obtain a better performance of the SWENSE method, we use a stricter definition of sharp interface, that is, the density is either the value of air or water without any transitional values. The density is determined using an original Heaviside function without any mollification. In other words, the transition thickness of the density is zero. In addition to the interface-capturing method, another difference between the present study and Li et al. (2019, 2021) is in the treatment of the additional term corresponding to the pressure of the incident flow. Here, this term is discretised explicitly instead of applying the GF method as in Li et al. (2019, 2021). Although the explicit calculation simplifies the implementation, additional treatment of the incident flow pressure is required to ensure numerical accuracy. The proposed method is found to be accurate in predicting the wave amplitude in different test cases, including wave propagation over a flat bottom, two-dimensional submerged breakwater, three-dimensional circular shoal, and with currents past a vertical cylinder. The remainder of this paper is organised as follows. Section 2 describes the governing equations and numerical methods. Section 3 discusses the test results of the four cases, followed by the conclusions in Section 4.

2. Numerical method

2.1. Field decomposition and governing equations

In the SWENSE method (Ferrant et al., 2003), the velocity $\boldsymbol{u}$ is decomposed as

$$\boldsymbol{u} = \boldsymbol{u}_I + \boldsymbol{u}_C, \tag{1}$$

where the subscripts I and C denote the incident and complementary fields, respectively. The pressure decomposition is expressed as (Li et al., 2021)

$$p = \frac{\rho}{\rho_I} p_I + p_C, \tag{2}$$

where ρ and ρ_I are the densities corresponding to the total and incident fields, respectively. The incident field can be regarded as a far field without considering the presence of solid bodies in the flow field, while the complementary field contains the irrotational flow induced by solid bodies and the rotational flow associated with viscous and wave breaking effects. Therefore, the air–water interfaces of the incident and total fields are typically not coincident. Thus, ρ and ρ_I in Eq. (2) can be different.

The incident field can be given by the potential theory as

$$\boldsymbol{u}_I = \nabla \varphi_I. \tag{3}$$

The potential function φ_I satisfies the Poisson equation, which can be solved analytically or numerically using a high-order accuracy scheme. Therefore, the wave amplitude of the incident field does not decay owing to the numerical dissipation in the Navier–Stokes equation solver. The incident field satisfies the following Euler equations for incompressible flow:

$$\nabla \cdot \boldsymbol{u}_I = 0, \tag{4}$$

$$\frac{\partial \boldsymbol{u}_I}{\partial t} + \boldsymbol{u}_I \cdot \nabla \boldsymbol{u}_I = -\frac{\nabla p_I}{\rho_I} + \boldsymbol{g}, \tag{5}$$

where t represents the time, $\boldsymbol{g}$ is the gravitational acceleration, and $\nabla = [\partial/\partial x, \partial/\partial y, \partial/\partial z]$ denotes the gradient operator. The pressure of the incident field p_I can be determined by the Euler equation (5) or equivalently, through the Bernoulli equation. The air–water interface of the incident field is assigned as the zero-value iso-surface of p_I.

Combining the following advection equation of density

$$\frac{\partial \rho}{\partial t} + \nabla \cdot (\rho \boldsymbol{u}) = \frac{\partial \rho}{\partial t} + \nabla \cdot (\rho \boldsymbol{u}_C) + \nabla \cdot (\rho \boldsymbol{u}_I) = 0, \tag{6}$$

the governing equation of $\rho \boldsymbol{u}_I$ can be derived as

$$\frac{\partial (\rho \boldsymbol{u}_I)}{\partial t} = -\nabla \cdot (\rho \boldsymbol{u}_I \boldsymbol{u}_I) - \boldsymbol{u}_I \nabla \cdot (\rho \boldsymbol{u}_C) - \frac{\rho}{\rho_I} \nabla p_I + \rho \boldsymbol{g}. \tag{7}$$

The difference between the governing equations of the total and incident fields yields the governing equations of the complementary field as

$$\nabla \cdot \boldsymbol{u}_C = 0, \tag{8}$$

$$\frac{\partial (\rho \boldsymbol{u}_C)}{\partial t} = -\nabla \cdot (\rho \boldsymbol{u} \boldsymbol{u}_C) - \nabla p_C + \nabla \cdot (2\mu \boldsymbol{S}) - \rho \nabla \cdot (\boldsymbol{u}_C \boldsymbol{u}_I) - \frac{p_I}{\rho_I} \nabla \rho, \tag{9}$$

where μ is the dynamic viscosity and $\boldsymbol{S} = (\nabla \boldsymbol{u} + \nabla \boldsymbol{u}^T)/2$ is the strain-rate tensor. The summation of Eqs. (5) and (9) results in the conservative form of the momentum equation of the total velocity $\boldsymbol{u}$. Eqs. (8) and (9) can be solved using the Navier–Stokes equation solver, with the last two terms in Eq. (9) treated as additional source terms.

2.2. Basic solver

In the present study, Eqs. (8) and (9) are solved using the in-house code developed in a previous study (Yang et al., 2021). The momentum equation is obtained using a fully explicit second-order Runge–Kutta (RK2) method. An adaptive time step is used. The time step determined using the Courant–Friedrichs–Lewy (CFL) number as

$$\Delta t = CFL \cdot min\left\{\frac{\Delta_x}{\boldsymbol{u}}, \frac{\Delta_y}{\boldsymbol{v}}, \frac{\Delta_z}{\boldsymbol{w}}, \frac{\rho \Delta^2}{6\mu}, \sqrt{\frac{\Delta_y}{g}}\right\} \tag{10}$$

where Δ_x, Δ_y and Δ_z represent the grid sizes in the x-, y-, z-directions, respectively, and $\Delta = (\Delta_x \Delta_y \Delta_z)^{1/3}$.

In each sub-step of the RK2 method, a fractional-step method (Kim and Moin, 1985) is applied to satisfy the divergence-free condition. To ensure the stability of the simulation, an approximation-synchronisation method is used to obtain the density field. In the approximation step, the density is estimated by solving the convection equation without considering the interface geometry. After a full time-step, the density is synchronised according to the interface location. The momentum is then updated using the synchronised density. Thus, the interface geometry is accurately captured.

The finite difference method is used to discretise the governing equations on a staggered Cartesian grid. The first three terms on the right-hand side of the momentum equation of $\boldsymbol{u}_C$ are similar to those in the governing equations of the total velocity $\boldsymbol{u}$. These three terms are discretised using the same scheme as that of the corresponding terms of $\boldsymbol{u}$. Therefore, the fundamental architecture of the basic solver does not require any modification. In particular, the convection term is estimated using a limited cubic upwind interpolation scheme (Patel and Natarajan, 2015), while the pressure and viscosity terms are calculated using a second-order central difference scheme.

The last two terms on the right-hand side of Eq. (9) are the additional terms of $\boldsymbol{u}_C$. To describe the spatial discretisation of these two terms, the coordinates of the cell centres are denoted as x_i, y_j, and z_k. The subscripts $i = 1, 2, \ldots, N_x$, $j = 1, 2, \ldots, N_y$, $k = 1, 2, \ldots, N_z$ represent the quantities defined at the cell centres in the x-, y-, z-directions, respectively. The velocity components in the corresponding directions are denoted by u, v, and w. Taking the equation in the x-direction as an example, the fourth term on the right-hand side of Eq. (9) is approximated as

$$\begin{aligned}
&-[\rho \nabla \cdot (\boldsymbol{u}_C \boldsymbol{u}_I)]_{i-1/2,j,k} \\
&= -\rho_{i-1/2,j,k} \frac{(u_C)_{i,j,k}(u_I)_{i,j,k} - (u_C)_{i-1,j,k}(u_I)_{i-1,j,k}}{\Delta_x} \\
&\quad - \rho_{i-1/2,j,k} \frac{(v_C)_{i-1/2,j+1/2,k}(u_I)_{i-1/2,j+1/2,k} - (v_C)_{i-1/2,j-1/2,k}(u_I)_{i-1/2,j-1/2,k}}{\Delta_y} \\
&\quad - \rho_{i-1/2,j,k} \frac{(w_C)_{i-1/2,j,k+1/2}(u_I)_{i-1/2,j,k+1/2} - (w_C)_{i-1/2,j,k-1/2}(u_I)_{i-1/2,j,k-1/2}}{\Delta_z}.
\end{aligned} \tag{11}$$

On a staggered grid, the velocity components are defined at the cell faces. The velocity components at the cell centres and edges in the above equation are calculated using a second-order central interpolation. The last term on the right-hand side of Eq. (9) is explicitly discretised using the following expression:

$$-\left[\frac{p_I}{\rho_I}\frac{\partial \rho}{\partial x}\right]_{i-1/2,j,k} = -\frac{(p_I)_{i-1/2,j,k}}{\rho_I}\frac{\rho_{i,j,k} - \rho_{i-1,j,k}}{\Delta x}. \tag{12}$$

The CLSVOF method is used to capture the interface between the two fluid phases by solving the following convection equations of the LS function ϕ and VOF function ψ:

$$\frac{\partial \phi}{\partial t} + \nabla \cdot (\phi \boldsymbol{u}) = 0, \tag{13}$$

$$\frac{\partial \psi}{\partial t} + \nabla \cdot (\psi \boldsymbol{u}) = 0, \tag{14}$$

In this paper, 'water' and 'air' are used to represent the two fluid phases. The LS function ϕ is defined as the signed distance from each cell centre to the air–water interface. Its sign is positive and negative in the water and air phases, respectively. The VOF function ψ is defined as the fraction of the volume occupied by water in each cell. Its value ranges from zero to one. To couple the LS and VOF functions, the LS function is used to determine the normal direction of the interface to reconstruct the interface in each grid cells in the VOF method. The VOF method ensures that the reconstructed interface satisfies the requirement of mass conservation. The reconstructed interface is then used to determine the LS function near the interface, which ensures the mass conservation of the LS function without applying any reinitialisation algorithms. Although the coupling of LS function increases the complexity of the interface-capturing algorithm, it does not influences the overall computational efficiency. This is because the CLSVOF method only costs 3%–4% computational time in the cases tested in the present study. Most computational time is used to solve the Poisson equation of the pressure, which occupies 70%–75% in the tested cases, and this percentage tends to increase as the number of grid points increases. In other words, the overall computational cost with the CLSVOF method is comparable to that with the VOF method.

Based on the LS function, the density ρ and dynamic viscosity μ are determined as

$$\rho = \rho_a + (\rho_w - \rho_a) H(\phi), \tag{15}$$

$$\mu = \mu_a + (\mu_w - \mu_a) H(\phi). \tag{16}$$

The Heaviside function $H(\phi)$ is defined as

$$H(\phi) = \begin{cases} 0 & , \quad \phi < 0 \\ 1 & , \quad \phi \geq 0 \end{cases}. \tag{17}$$

From Eq. (17), it is understood that the density and viscosity change sharply across the interface without applying any diffusion. The application of the sharp-interface treatment improves the accuracy of the momentum flux calculation around the interface. However, when coupled with the SWENSE method, the calculation of p_I in Eq. (12) must be treated carefully, which is discussed in Section 2.3.

2.3. Pressure translation correction

An intuitive approach to calculate $(p_I)_{i-1/2,j,k}$ in Eq. (12) is to interpolate it using p_I at the two neighbouring cell centres. However, this treatment causes numerical inaccuracy. Fig. 1 demonstrates this point. The figure shows a special condition $\boldsymbol{u}_C = 0$, under which the interfaces corresponding to $\boldsymbol{u}$ (the edge of the grey area) and $\boldsymbol{u}_I$ (the dashed line) are expected to collapse. If the viscosity is negligible, then the first four terms on the right-hand side of Eq. (9) are all zero. The fifth term is also trivial at the cell faces away from the interface because of the condition $\partial \rho / \partial x = 0$. At a cell face next to the interface, taking point A in Fig. 1 as an example, $\partial \rho / \partial x$ is non-trivial. If p_I is determined by interpolation, then it is also non-trivial at point A. This is because $p_I = 0$ is satisfied at the interface of the incident field, which is usually not collocated with the cell face centres. This means that the last term is not zero, which acts as a non-physical momentum source causing spurious velocity.

To address this issue, we revisit Eq. (9) in a continuum framework. The last term can be regarded as a surface force, which is only non-trivial at the interface of the total field. In a discretised system, it must

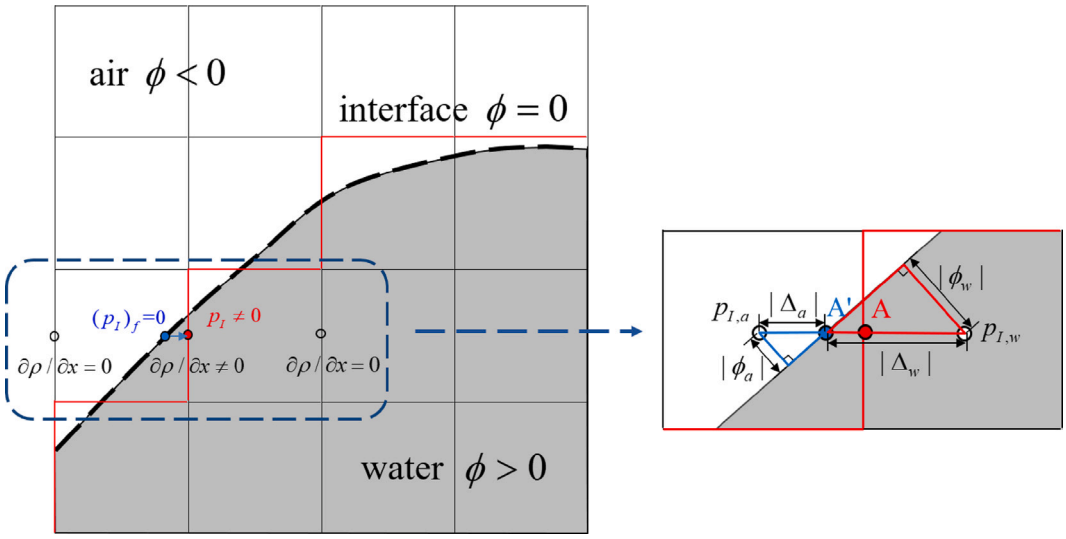

Fig. 1. The sketch of the operation of pressure translation correction.

be redistributed to the neighbouring cell faces. In the present study, we calculated this term at point A' and prescribed its value to point A. This treatment is equivalent to translating p_I at point A' to correct its value at point A. Therefore, it is called the pressure translation correction (PTC) method. The calculation of p_I at point A' is given by a linear interpolation as

$$p_I = \frac{p_{I,w}\Delta_a + p_{I,a}\Delta_w}{\Delta_w + \Delta_a}. \tag{18}$$

where $p_{I,w}$ and $p_{I,a}$ are the pressures at two neighbouring cell centres in the water and air phases, respectively; and Δ_w and Δ_a are the distances between the corresponding cell centres and the interface. In the present framework, based on the CLSVOF method, the interface is defined as $\phi = 0$, the location of which can be determined by interpolating the LS function ϕ at the cell centres. Specifically, it is assumed that the curvature radius of the interface is significantly larger than the grid size, such that the interfaces inside two adjacent cells are approximately in the same plane. As shown in the right panel of Fig. 1, the ratio between Δ_w and Δ_a can be estimated as

$$\frac{\Delta_w}{\Delta_a} \approx \frac{|\phi_w|}{|\phi_a|} \tag{19}$$

Substituting Eq. (19) into Eq. (18) results in the following estimation of p_I at point A'.

$$p_I = \frac{p_{I,w} + p_{I,a}\frac{\Delta_w}{\Delta_a}}{1 + \frac{\Delta_a}{\Delta_w}} \approx \frac{p_{I,w} + p_{I,a}\frac{|\phi_w|}{|\phi_a|}}{1 + \frac{|\phi_a|}{|\phi_w|}} = \frac{p_{I,w}|\phi_a| + p_{I,a}|\phi_w|}{|\phi_w| + |\phi_a|}. \tag{20}$$

Based on the above treatment, the special condition $\boldsymbol{u}_C = 0$ can be reconsidered as follows. Because $p_I = 0$ is defined at point A', $p_I = 0$ is also satisfied at point A with the PTC method. This is a desirable feature because it ensures that the last term on the right-hand side of Eq. (9) is trivial when it should be. If a disturbance exists in the flow field, the air–water interface corresponding to the total field $\boldsymbol{u}$ deviates from that corresponding to the incident field $\boldsymbol{u}_I$. Under this condition, p_I at point A' becomes non-trivial (note that point A' is located at the air–water interface of the total field, but not the incident field). The presence of the disturbance is received by the complementary field $\boldsymbol{u}_C$.

From the perspective of a discretised system, the PTC method is a zeroth-order accuracy approximation of the last term in Eq. (9). This is because no higher-order term of the grid size Δ is explicitly involved in the relationship between the values of p_I at points A and A'. We do not intend to seek a higher-order approximation for the following reasons. First, the PTC method satisfies the most fundamental requirement (i.e. p_I is equal to zero when it should be) under the special condition $\boldsymbol{u}_C = 0$. Second, a higher-order scheme requires the gradient of p_I, which is likely to introduce additional error sources into the system. Finally, the last term is only non-trivial in the flow regions where the interface of the real field does not collocate with the incident field. In the SWENSE method, the grid resolution in these regions must be refined to capture the disturbance effect of $\boldsymbol{u}_C$. Therefore, the discretisation error associated with the PTC method is not dominant. The test results in Section 3.1 show that the zeroth-order approximation is sufficiently accurate to predict the interface geometry.

To finalise the discussion of the PTC method, we note that in the previous study by Li et al. (2019), it is shown that the direct interpolation of p_I to cell faces without applying any correction yields reasonable results of the interface geometry when the interface is diffused within several cells. However, the density gradient has a larger value in the present study owing to the sharp-interface treatment, which increases the sensitivity of the simulation results to the error in p_I. The test results in Section 3 show that applying the PTC method with the sharp interface is required in the present framework. Although additional treatment is required in the calculation of p_I, it does not essentially increase the complexity of the code implementation, while the accuracy of the interface geometry is improved with the sharp-interface treatment.

2.4. Boundary conditions

A periodic boundary condition is prescribed in the wave propagation direction. Relaxation zones (Jacobsen et al., 2012) are applied to both sides of the computational domain in the wave propagation direction. In the relaxation zone, the complementary field is damped out and only the incident field is sustained. At the top and side boundaries, a free-slip condition is applied to the complementary field, same as the previous study (Li et al., 2021). At the bottom, the boundary condition of the total field can be either no-slip or free-slip.

Owing to the use of a Cartesian grid, the immersed boundary (IB) method is used to capture the geometry of solid bodies inside the computational domain. In this study, we adopt the sharp-interface IB method described in Cui et al. (2018). Note that the no-slip boundary condition must be satisfied by the total field, but not the complementary field. In fact, the incident field is given without considering the presence of any solid bodies; thus, it does not satisfy the no-slip boundary condition at the body surfaces. Therefore, the boundary condition of the complementary field should be the opposite of incident field rather than no-slip at the surfaces of immersed bodies.

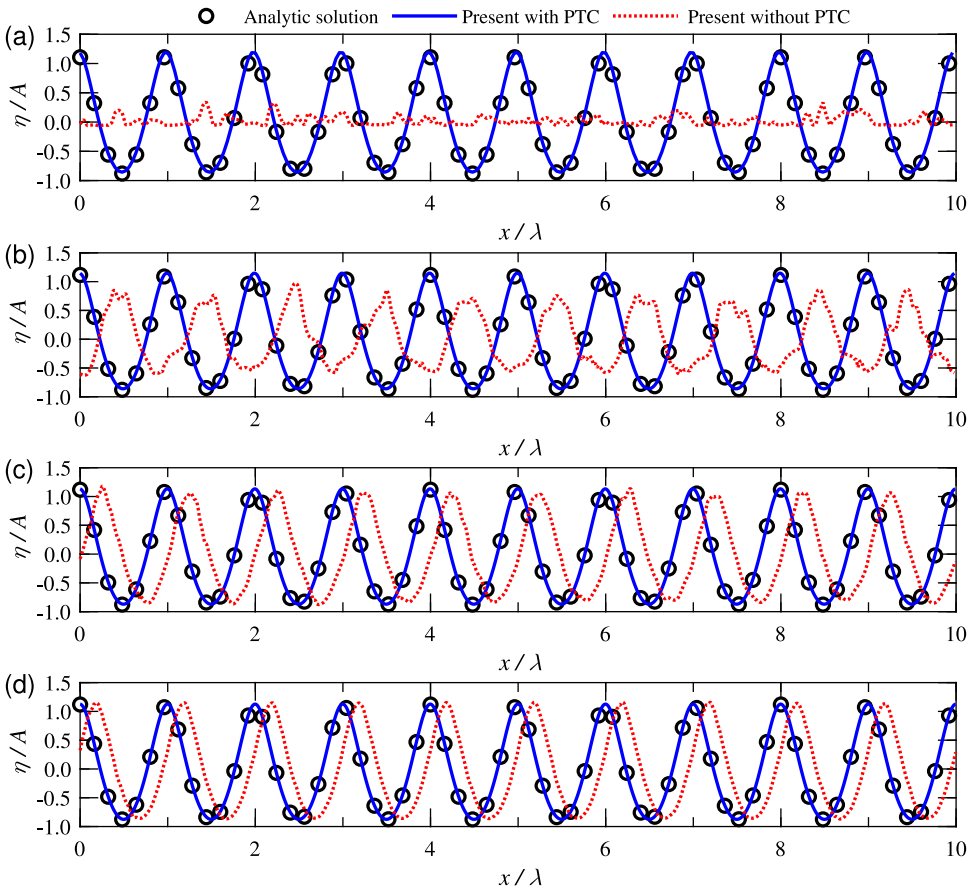

Fig. 2. Wave geometry at $t = 20T$ in the test case of wave propagation over a flat bottom. The number of grid points is (a) 256 × 64, (b) 500 × 128, (c) 1000 × 256, and (d) 2000 × 512.

Table 1
Physical parameters of the incident waves for the test case of wave propagation over a flat bottom.

Parameter	Value
Wave height ($2a/\lambda$)	0.0711
Water steepness (ka)	0.2235
Water depth (h/λ)	0.7425
Dispersion parameter (kh)	4.6645
Wave phase speed ($c/\sqrt{g\lambda}$)	0.4090
Wave period ($T/\sqrt{\lambda/g}$)	2.4447

Table 2
Grid parameters for the test case of wave propagation over a flat bottom.

	Very coarse	Coarse	Medium	Fine
N_x	250	500	1000	2000
N_y	64	128	256	512
Δx	$\lambda/25$	$\lambda/50$	$\lambda/100$	$\lambda/200$
Δy	$H/5$	$H/10$	$H/20$	$H/40$

3. Test results

3.1. Wave propagation over a flat bottom

In the first test case, two-dimensional deep-water gravity waves are analytically obtained using a stream function solution as the incident field (Rienecker and Fenton, 1981). The bottom is flat and the flow field has no structure. The flow is inviscid. Thus, the complementary field should be zero, and the wave geometry of the total field should be consistent with the incident field. This is the most fundamental case for examining the accuracy and robustness of the SWENSE method.

Table 1 lists the physical parameters of the incident waves. The wave amplitude is $a = 0.0711\lambda$, where λ is the wavelength of the incident field, yielding a wave steepness of $ka = 0.2235$. The water depth is $h = 0.7425\lambda$, yielding a dispersion parameter of $kh = 4.665$ that satisfies the deep-water condition. The wave phase speed is $c = 0.4090\sqrt{g\lambda}$, and the wave period is $T = \lambda/c = 2.4447\sqrt{\lambda/g}$. The above parameters of the incident waves are also used to initialise the simulation. All the physical parameters in this test case are consistent with those in Li et al. (2021) to facilitate a direct comparison with their results.

The computational domain size is $L_x \times L_y = 10\lambda \times 0.92\lambda$. The tests are conducted using different grid resolutions. Table 2 lists the number of grid points and grid resolution for different tests. It can be seen that the number of grid points is $N_x \times N_y = 250n \times 64n$, where n is 1, 2, 4, and 8. On the coarsest grid with $n = 1$ and finest grid with $n = 8$, the grid resolutions are $\Delta_x \times \Delta_y = \lambda/25 \times H/5$ and $\lambda/200 \times H/40$, respectively, where $H = 2a$ is the wave height.

First, we demonstrate the importance of applying the PTC method described in Section 2.3. Fig. 2 compares the wave geometries at $T = 20$ obtained from the simulations with and without the application of the PTC method. The analytical solution is also shown in the figure. It can be seen that when the PTC method is applied, the numerical results agree with the analytical solution on the coarsest grid. In contrast, the wave amplitude is significantly underestimated on the coarsest grid when the PTC method is not applied. As the number of grid points increases, the wave amplitudes obtained without applying the PTC method approach the analytical value; however, the error in the wave

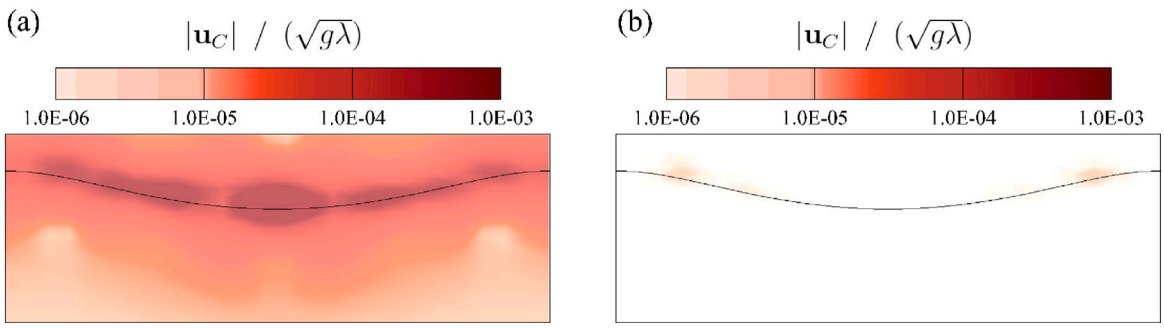

Fig. 3. Complementary velocity fields (a) without and (b) with the use of the PTC method after the first time step.

Table 3
Relative errors of the numerical results with respect to the analytical solution in the first-order wave amplitude for the test case of wave propagation over a flat bottom at $t = 20T$.

N_y	Present with PTC	Present without PTC	Li et al. (2021)
64	+2.62%	−93.77%	——
128	+0.53%	−38.20%	−2.45%
256	+0.15%	−6.58%	−0.81%
512	+0.06%	−1.23%	−1.03%

Table 4
Relative errors of the numerical results with respect to the analytical solution in the second-order wave amplitude for the test case of wave propagation over a flat bottom at $t = 20T$.

N_y	Present with PTC	Present without PTC	Li et al. (2021)
64	+5.17%	−55.04%	——
128	+1.47%	+35.21%	−3.96%
256	+0.27%	−4.81%	−1.80%
512	+0.09%	+7.56%	−1.96%

phase cannot be eliminated. Thus, applying the PTC method is crucial to obtaining accurate results of the wave geometry.

To further visualise the effects of the PTC method, Fig. 3 compares the complementary velocity fields obtained from the simulations without and with the use of the PTC method after the first time step. The black lines demarcate the water surface. It is seen from Fig. 3(a) that a large magnitude of spurious velocity that reaches a maximum of $3.69 \times 10^{-3}\sqrt{g\lambda}$ is generated near the interface without using the PTC method. This spurious velocity is significantly reduced by more than 99% with the use of the PTC method, as shown in Fig. 3(b). This allows the regular wave to propagate accurately. The results in Fig. 3 indicates that the PTC method eliminates the spurious velocity. This is crucial for the accurate prediction of the wave geometry in the present SWENSE method coupled to the CLSVOF method.

Fig. 4 compares the results of the first- and second-order wave amplitudes $\eta^{(1)}$ and $\eta^{(2)}$ with Li et al. (2021). The wave amplitudes are defined as

$$\eta^{(1)} = \sum_{j=1}^{n} \eta(j) e^{-i\frac{2\pi j}{n}}, \eta^{(2)} = \sum_{j=1}^{n} \eta(j) e^{-i\frac{4\pi j}{n}}. \tag{21}$$

The results are normalised using the corresponding analytical values $\eta_0^{(1)}$ and $\eta_0^{(2)}$. To facilitate a quantitative comparison, Tables 3 and 4 list the relative errors in the first- and second-order amplitudes at $t = 20T$, respectively. It is evident from Fig. 4 and Tables 3 and 4 that the present results are closer to the analytical solution than those of Li et al. (2021). This is mainly attributed to the accurate identification of the interface location in the present study based on the LS function. Specifically, the value of P_I at the interface needs to be calculated, which requires to allocate the interface first. In the study by Li et al. (2021), the interface was captured using the VOF method, and the location of the interface could only be approximated by $\psi = 0.5$. Additionally, P_I was computed on the cell face closest to the isosurface of $\psi = 0.5$, rather than on the isosurface as in the present study, resulting in a first-order discretisation error with respect to the grid size. In the present method, the interface location is determined using the LS function as illustrated in Fig. 1. This provides a more accurate estimation of P_I at the interface. Therefore, the coupling of the LS function can be regarded as the key for improving the accuracy of the SWENSE method in the present study over the previous method of Li et al. (2021).

Fig. 4 shows another desirable feature of the present results: the error decreases as the grid is refined. To further examine the numerical accuracy, Fig. 5 shows the error in the wave amplitude at $t = 20T$ based on different numbers of grid points. The error is defined as

$$E(\eta) = \frac{\eta_s^n - \eta_a^t}{\eta_a^n}, \tag{22}$$

where the subscripts s and a denote the simulation and analytical results, respectively. Because the grid resolution is proportionally refined in two directions in the present tests, the number of grid points in the vertical direction N_y is used as a representative of the grid resolution in Fig. 5. The slope is fitted using the least-squares method. It can be seen that for both $\eta^{(1)}$ and $\eta^{(2)}$, the accuracy is slightly lower but close to the second order. These results indicate that although the PTC method is only a zeroth-order approximation, it can accurately predict the wave geometry. Thus, a high-order scheme is unnecessary.

The above tests are conducted on a uniform grid. In many applications, it is common to refine the mesh near the water surface and structures, and stretch the grid to the boundaries to reduce the computational cost. As a result, we also test the proposed SWENSE method in a non-uniform grid. In this test, we remain the computational domain size the same as the previous test. The grid resolution at the central region also remains unchanged. Specifically, in a sub-domain $[3\lambda, 7\lambda] \times [h - 0.8H, h + 0.8H]$, the grid resolution is $\Delta_x \times \Delta_y = \lambda/(25n) \times H/(5n)$, where n is 2, 4, and 8. The grid size is stretched to the four boundaries of the computational domain. This treatment reduces the number of grid points from $N_x \times N_y = 250n \times 64n$ for the previous uniform grid to $N_x \times N_y = 200n \times 28n$ for the present non-uniform grid.

Fig. 6 compares the first- and second-order wave amplitudes $\eta^{(1)}$ and $\eta^{(2)}$ normalised by the corresponding analytical values obtained from uniform and non-uniform grids. It is seen that when a low grid resolution of $\Delta_y = H/10$ is used, the non-uniform grid over-predicts the second-order wave amplitude. As the grid resolution is refined to $\Delta_y = H/20$ and $\Delta_y = H/40$, the difference between non-uniform and uniform grids becomes insignificant. The test results shown in Fig. 6 indicate that using the non-uniform grid provides the same accuracy in the wave amplitude as the uniform grid by using only 34% grid points.

3.2. Wave propagation over a two-dimensional submerged breakwater

The above test of the wave propagation over a flat bottom shows the accuracy of the proposed method without the presence of a complementary field. In the following tests, we further examine the performance

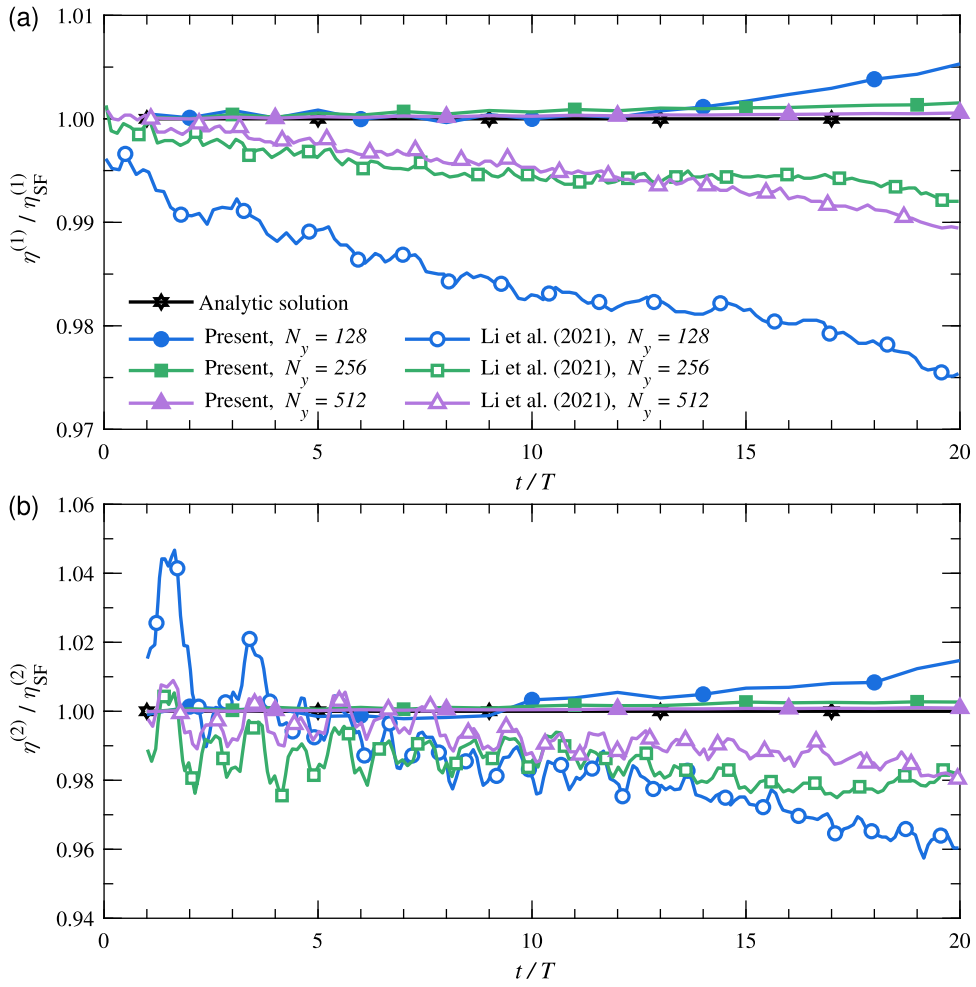

Fig. 4. Time evolution of the normalised (a) first-order and (b) second-order wave amplitude obtained from the present simulation. Previous results of Li et al. (2021) are shown for comparison.

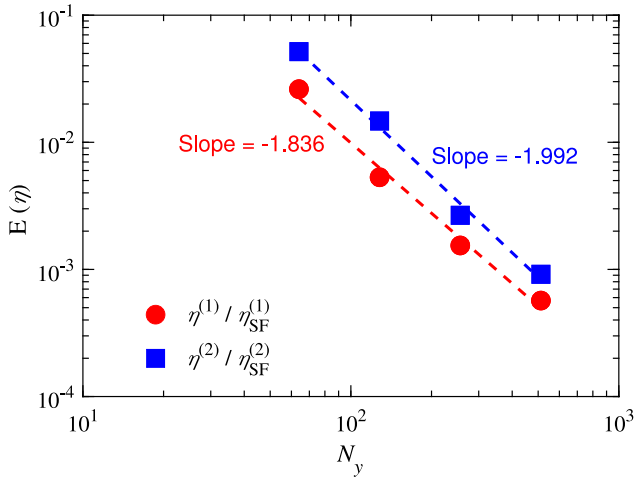

Fig. 5. Relative error in the first- and second-order wave amplitude at $t = 20T$ for the test case of wave propagation over a flat bottom.

of this method in capturing the effects of various solid body structures on the wave propagation. We begin with the case of wave propagation over a two-dimensional submerged breakwater. This case was experimentally investigated by Luth et al. (1994), and was used as a benchmark to examine the performance of numerical simulations (Gobbi and Kirby, 1999; Engsig-Karup et al., 2006; Zhao et al., 2015b; Chen and Hsiao, 2016).

Fig. 7 shows a schematic of the test case. The computational domain size is $L_x \times L_y = 44.88\ \text{m} \times 0.6\ \text{m}$, where x and y represent the wave propagation and vertical directions, respectively. The water depth is 0.4 m. The breakwater is located from $x = 6$ m to 17 m. The breakwater height is 0.3 m; hence, the water depth is reduced to 0.1 m over the top of the breakwater. The slopes of the front and back faces are 1 : 20 and 1 : 10, respectively. The wavelength, height, and phase speed of the incident waves are $\lambda = 3.74$ m, 0.02 m, and 1.85 m/s, respectively. These parameters are also used to generate the initial waves of the simulation. The relaxation zones are located at the left and right boundaries. The width of each relaxation zone is twice the wavelength (i.e. 7.48 m). The number of grid points is $N_x \times N_y = 1536 \times 256$, providing a grid resolution of $\Delta_x \times \Delta_y = 0.0292\ \text{m} \times 0.00235$ m.

We recorded the time histories of the water surface elevations at different points (Fig. 7) for comparison with the experimental data (Luth et al., 1994). The results are shown in Fig. 8. The relative errors of the numerical simulation with respect to the experimental data in the maximum of water elevation at different locations are given quantitatively in Table 5. As shown in Fig. 8, when the waves approach

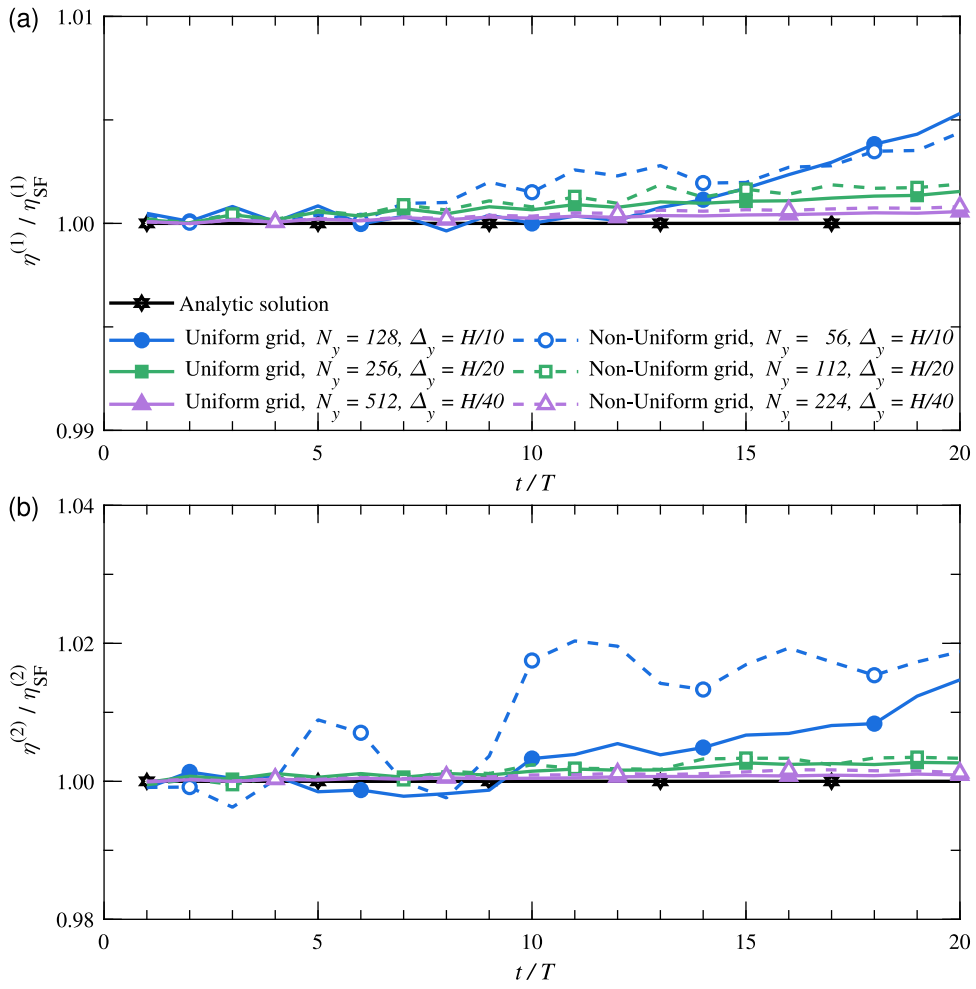

Fig. 6. Time evolution of the normalised (a) first-order and (b) second-order wave amplitude obtained from a non-uniform grid. The results obtained from a uniform grid are shown for comparison.

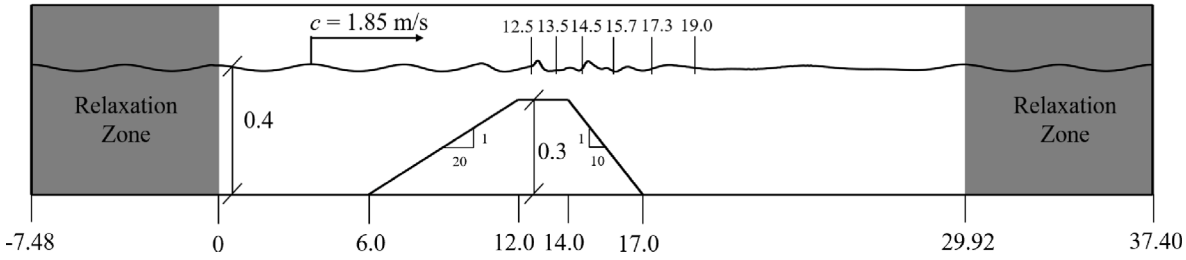

Fig. 7. Sketch of key simulation parameters for the test case of wave propagation over a two-dimensional submerged breakwater. The unit of all length scales is metre.

Table 5
Relative errors of the numerical simulation with respect to the experimental data in the maximum of water elevation at different locations for the test case of wave propagation over a two-dimensional submerged breakwater.

Location	Present with PTC	Present without PTC
x = 12.5 m	+0.90%	−27.00%
x = 13.5 m	−2.19%	−29.47%
x = 14.5 m	−1.98%	−27.45%
x = 15.7 m	−4.44%	−20.07%
x = 17.3 m	+4.84%	−17.83%
x = 19.0 m	+4.74%	−28.42%

the bar, the water depth decreases. The nonlinearity of the wave is enhanced (Jacobsen, 2011), and the wave amplitude reaches a maximum at the top of the bar. When the waves propagate over the bar, the water depth increases and the wave amplitude decreases. It is seen from both Fig. 8 and Table 5 that when the PTC method is adopted, the numerical results agree with the experimental results at all monitoring points. In contrast, without the PTC method, the wave amplitude is underestimated.

3.3. Wave propagation over a submerged circular shoal

In this test, we examine the capability of the proposed method to simulate three-dimensional cases. The test is conducted in the context of wave propagation over a submerged circular shoal. This case was

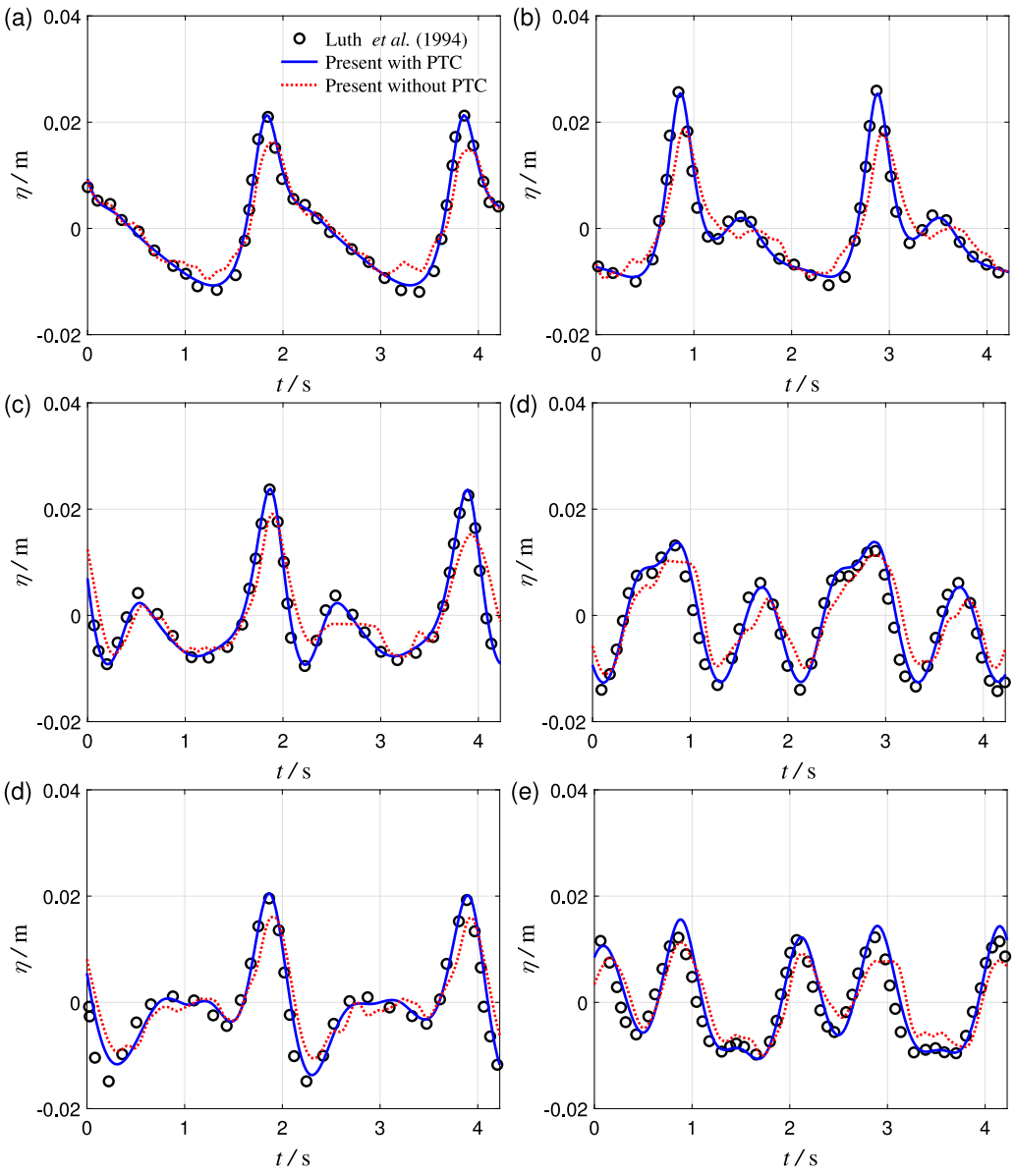

Fig. 8. Time evolution of the water elevation or the test case of wave propagation over a two-dimensional breakwater at different locations: (a) $x = 12.5$ m, (b) $x = 13.5$ m, (c) $x = 14.5$ m, (d) $x = 15.7$ m, (e) $x = 17.3$ m, and (f) $x = 19.0$ m.

studied experimentally by Chawla and Kirby (1996), and was considered by Chen et al. (2000) and Zhao et al. (2015a) to validate their simulations based on the potential theory. Similar experiments were conducted by Lee et al. (2013).

Fig. 9 shows the top view of the computational domain for this test case. The coordinates x, y and z denote the wave propagation, lateral, and vertical directions, respectively. The computational domain is $L_x \times L_y \times L_z = 30$ m$\times 18.2$ m$\times 0.75$ m. The water depth is $h_0 = 0.45$ m. The shoal geometry is a spherical crown. Its centre is located at $x = 5$ m and $y = 8.98$ m. The radius of the crown is 9.1 m. At the bottom, the outer border of the crown is expressed as

$$(x-5)^2 + (y-8.98)^2 = (2.57)^2. \tag{23}$$

The water depth over the circular shoal is given as

$$h = h_0 + 8.73 - \sqrt{82.81 - (x-5)^2 - (y-8.98)^2}, \tag{24}$$

which results in a minimum water depth of 0.08 m over the top of the crown. The wavelength, wave height, and phase speed of the incident wave are $\lambda = 1.5$ m, $H_0 = 1.18$ cm, and $c = 1.5$ m/s, respectively. The initial wave geometry remains the same as the incident wave. The relaxation zones are located at the two sides of the computational domain in the x-direction. The width of the relaxation zone is 3 m, which is twice the wavelength. The number of grid points is $N_x \times N_y \times N_z = 600 \times 360 \times 200$. The grid resolution is 0.05 m in the x- and y-directions, respectively. In the vertical (z) direction, The grid is refined near the water surface from $z = 0.37$ m to 0.52 m, where the grid resolution is $\Delta_z = 0.0012$ m. The grid is stretch to the top and bottom boundaries of the computational domain. The grid is displayed in Fig. 10. The simulation parameters are consistent with those in the experiment of Chawla and Kirby (1996).

Fig. 11 shows the instantaneous water surface at $t = 10T$, where $T = \lambda/c = 1$s denotes the wave period. It is observed that the waves refract over the shoal owing to the change in wave depth. The wave amplitude is attenuated as it propagates over the shoal. The wave geometry shown in Fig. 11 is qualitatively consistent with the observations from previous studies (Lee et al., 2013; Zhao et al., 2010).

To further validate the simulation results quantitatively, the wave amplitudes along different longitudinal and lateral lines are collected.

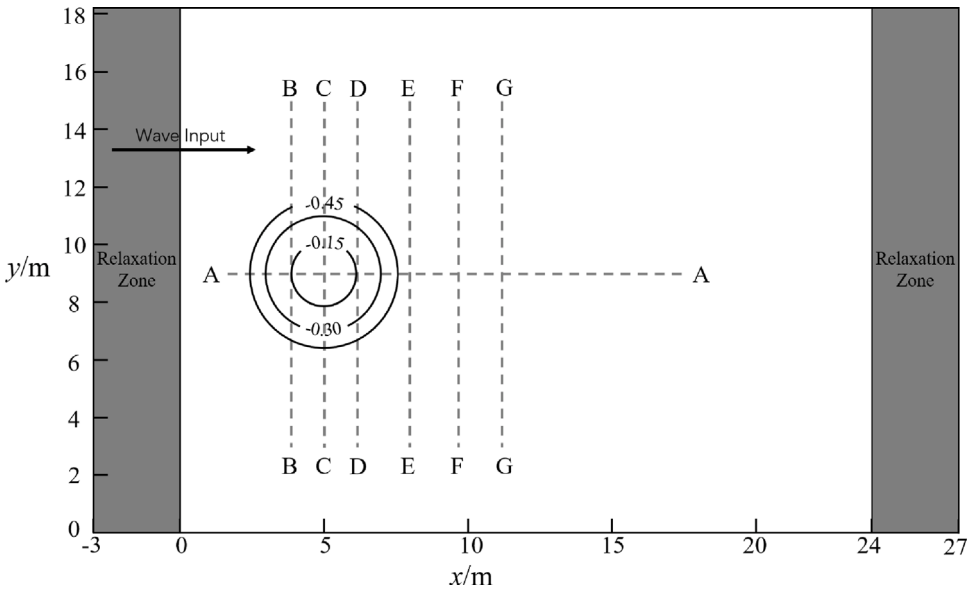

Fig. 9. Top-view sketch of key simulation parameters for the test case of wave propagation over a circular submerged shoal. The unit of all lengths scales is metre. The solid circles represent the isopleths of the shoal with the altitude marked by the numbers. The mean water elevation is defined as $z = 0$. The coordinates x, y and z denote the wave propagation, lateral, and vertical directions, respectively.

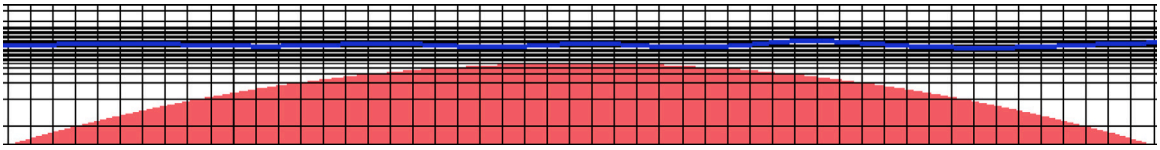

Fig. 10. Front-view of grid diagram around the shoal. To facilitate a clear illustration, only 1/2 grid lines and 1/8 grid lines are displayed in the x- and z-directions, respectively. The red curves illustrate the free surface position at $t = 10T$.

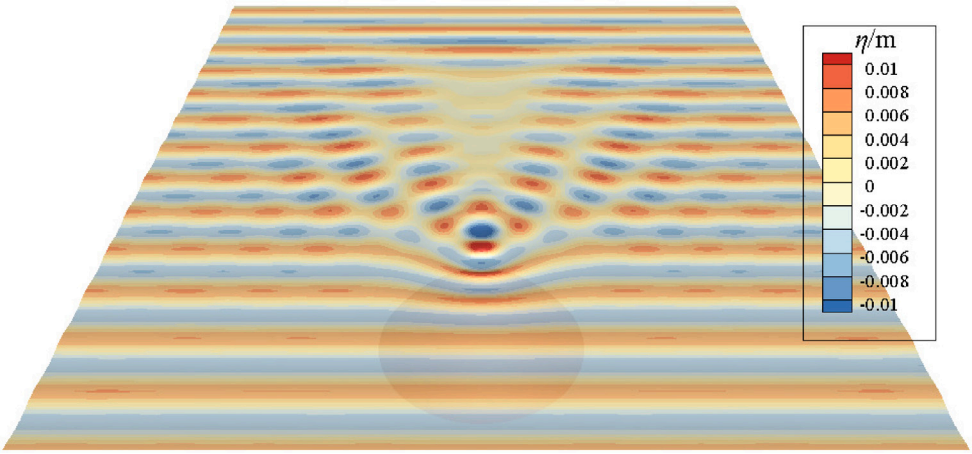

Fig. 11. Wave geometry at $t = 10T$ in the test case of a regular wave over a 3D submerged shoal. The contour shows the water elevation.

The locations of these lines are shown in Fig. 9. The simulation results are compared with the experimental data in Fig. 12. It is seen that the simulation results generally agree with the experimental results when the PTC method is adopted. If the PTC method is not adopted, the wave amplitude is underestimated by the numerical simulation. In particular, as shown in Fig. 12(a), the maximum wave amplitude predicted by the numerical simulation with the PTC method is $H = 2.7H_0$, which occurs at $x = 8.0$ m. The relative error of this maximum wave amplitude is 2.92% with respect to the measurement. However, if the PTC method is not applied, the maximum wave amplitude is underestimated as $H = 2.2H_0$, of which the relative error increases to −11.97%. This indicates that the PTC method improves the accuracy of the wave amplitude, particularly when the wave nonlinearity is strong. Furthermore, the simulation results are oscillatory without the PTC method. This is evident in the insets in Fig. 12(f,g). This observation indicates that without the PTC method, spurious velocity is induced.

3.4. Wave propagation with currents past a vertical circular cylinder

In the above test cases, the complementary field is essentially a potential flow corresponding to the submerged solid bodies. Therefore, the wave geometries in these cases can be accurately predicted by a

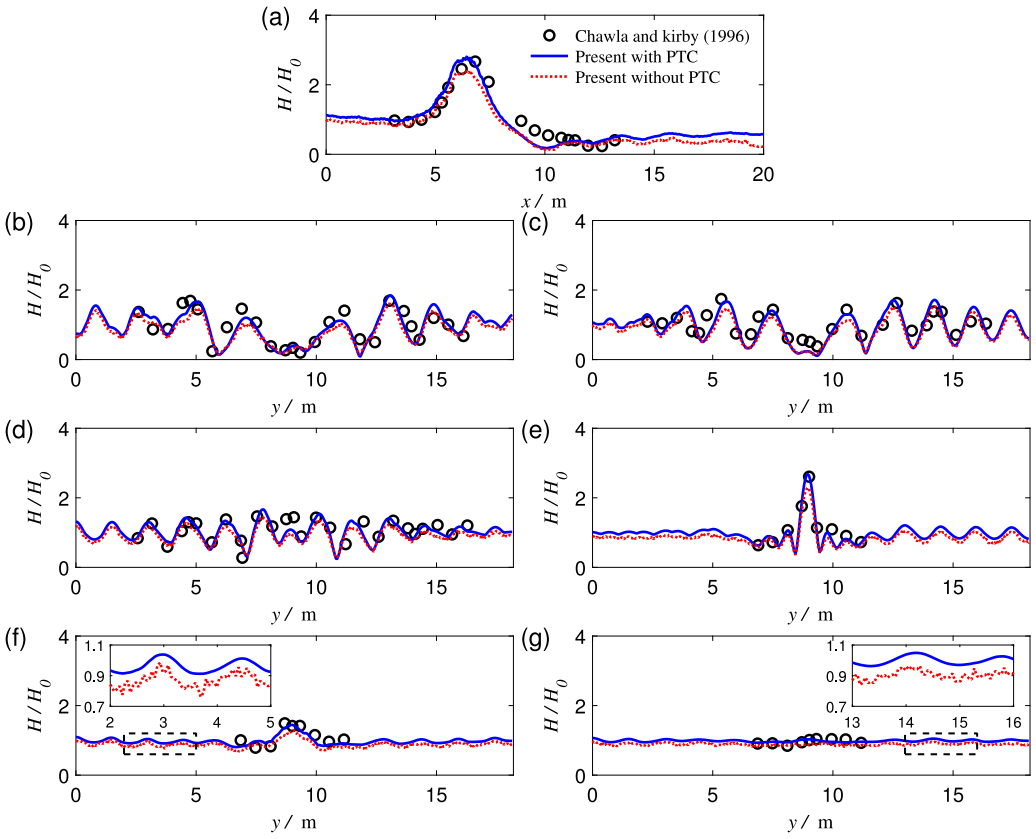

Fig. 12. Wave amplitude along different longitudinal and lateral lines for the test case of wave propagation over a circular shoal. The locations of the lines correspond to (a) A–A, (b) B–B, (c) C–C, (d) D–D, (e) E–E, (f) F–F, and (g) G–G, as shown in Fig. 9.

potential flow solver (Gobbi and Kirby, 1999; Zhao et al., 2015b; Chen et al., 2000; Zhao et al., 2019). As a potential–viscous coupling method, the SWENSE method have shown its low numerical dissipation and dispersion performance in the previous potential problem test cases. Meanwhile, owing to the coupling of potential-flow solution to the viscous-flow solver, the SWENSE method has another advantage, that is, its ability in simulating viscous flow phenomena, such as vortex shedding in flow past a bluff body. To demonstrate this, we conducted a test case of wave propagation with currents past a vertical circular cylinder. It should be noted that there are no benchmark experiments for this test case in the literature. Therefore, we are unable to quantitatively validate our simulation results. The purpose of conducting this test case is to demonstrate the capability of the proposed method in resolving the rotational flow in a qualitative manner.

Fig. 13 shows the side and top views of the computational domain. The computational domain size is $L_x \times L_y \times L_z = 17\lambda \times 8\lambda \times 1.4\lambda$, where λ represents the wavelength of the incident wave. The water depth is $h_0 = \lambda$. The steepness of the incident wave is $ka = 0.20$, where $k = 2\pi/\lambda$ and a is the wavenumber and wave amplitude, respectively. The current velocity is $U_c = 0.273c$, where c is the wave phase speed. The cylinder diameter $D = \lambda/2$ is one-half the wavelength. Its centre is located 4λ from the left boundary. The Reynolds number is $Re = U_c\lambda/\nu = 3900$. The number of grid points is $N_x \times N_y \times N_z = 200 \times 160 \times 140$.

Fig. 14 shows the instantaneous surface geometry and vortex structures visualised using the iso-surface of $\phi = 0$ and $Q = 0.2U_c^2/\lambda^2$, respectively, where Q is the vortex identification criterion (Hunt et al., 1988). As shown in Fig. 14, the interface geometry is disturbed downstream of the cylinder. Owing to the no-slip boundary condition applied at the bottom boundary, a horseshoe vortex appears at the junction between the front of the cylinder and the bottom. This observation is consistent with the results of Shin et al. (2017). Behind the cylinder, irregular vortex shedding is observed, indicating the presence of viscous effect. This observation indicates that the proposed method can solve rotational flows.

4. Conclusion

In this study, we describe a wave generation algorithm based on a velocity decomposition strategy for interface-resolved two-phase flow simulations. Unlike previous methods based on velocity decomposition, the additional source term associated with the pressure of the incident field is explicitly discretised. Although the explicit calculation of the source term simplifies the implementation, the simulation results are sensitive to the calculation method of the incident pressure. If the pressure at the cell faces is directly used to calculate the additional source term, a spurious velocity is induced. To improve the numerical accuracy, we propose a pressure translation correlation method, in which the pressure of the incident field is calculated at the wave surface and prescribed to the adjacent cell faces. This method eliminates the spurious velocity and improves the numerical accuracy. Another difference between the proposed method and the previous study is the interface-capturing method. The proposed method is developed within the framework of the CLSVOF method. The interface location is accurately identified with the aid of the LS function. Consequently, the calculation of the source term is also more accurate.

The proposed method is quantitatively validated in three test cases. In the first test case of wave propagation over a flat bottom, the incident field is theoretically zero, and the simulation results are compared

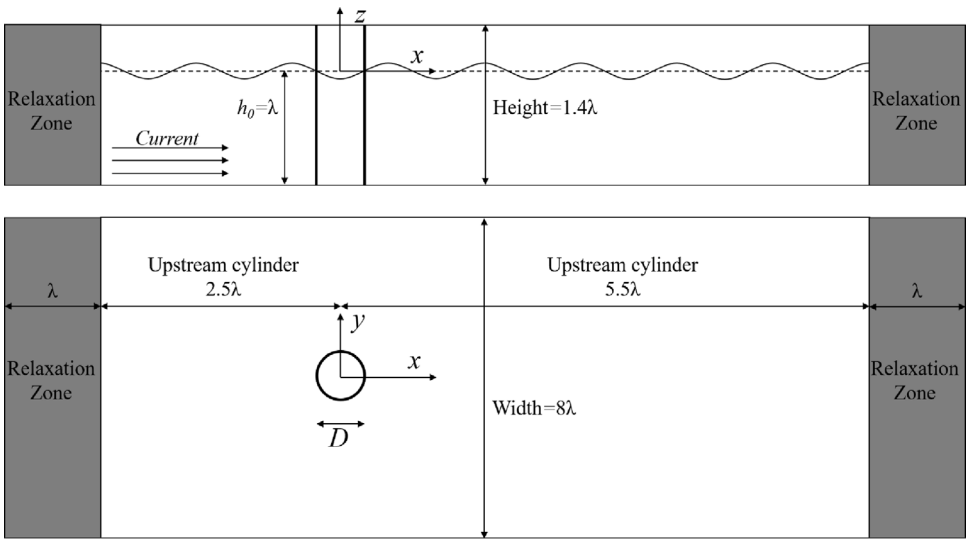

Fig. 13. Sketch of the computational domain for the test case of wave propagation with currents flow past a vertical circular cylinder.

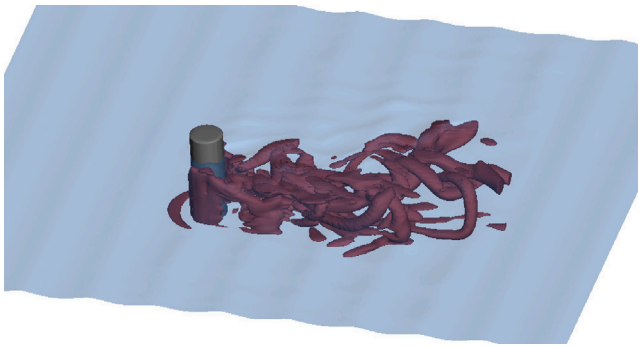

Fig. 14. Instantaneous surface geometry and vortex structures visualised using the iso-surfaces of $\phi = 0$ and $Q = 0.2U_c^2/\lambda^2$, respectively, for the test case of wave propagation with currents past a vertical circular cylinder.

with the analytical solution. This test case shows that owing to the coupling of the LS function for interface capture, the present results are more accurate than those in the literature that identify the interface using the VOF function. The numerical results of the wave amplitude show second-order spatial accuracy in a resolution-convergence test, a desirable feature that was not achieved in a previous wave generation methods based on the velocity decomposition strategy. In the second test case of wave propagation over two- and three-dimensional submerged objects, the simulation results show good agreement with experimental results reported in the literature. The last test case involves a wave propagation with currents past a circular cylinder. This case demonstrates the ability of the proposed method in simulating viscous effect, which cannot be achieved by a potential flow solver.

In present method, it is assumed that the interface in two adjacent grids remain in the same plane. This assumption is correct if the curvature radius of the interface is smaller than the grid size. If large deformation occurs in the interface, this assumption is incorrect. Therefore, the proposed method cannot be used to simulate problems with breaking waves. This issue can be addressed by locally refining the mesh. Therefore, adaptive mesh refinement technique (Sussman et al., 1999; Popinet, 2009; Zeng et al., 2022a,b, 2023) is expected to be a potential solution. At the same time, the use of adaptive mesh also helps to highlight the advantage of the SWENSE method in using a coarse mesh in the far field, such that accurate simulations of wave–structure interaction problems can be achieved using less computational resources.

CRediT authorship contribution statement

Tietao Lao: Investigation, Validation, Formal analysis, Writing – original draft. **Zhaobin Li:** Methodology, Conceptualization, Formal Analysis. **Zhiying Wang:** Supervision, Validation, Supervision. **Zhan Wang:** Project Administration, Writing – review & editing. **Zixuan Yang:** Conceptualization, Writing – review & editing, Supervision, Project administration.

Declaration of competing interest

The authors declare that they have no known competing financial interests or personal relationships that could have appeared to influence the work reported in this paper.

Data availability

Data will be made available on request

Acknowledgements

This research is supported by the National Natural Science Foundation of China (NSFC) Basic Science Center Program for Multiscale Problems in Nonlinear Mechanics' (No. 11988102) and NSFC, China project (No. 11972038, 11902323, 12202453).

References

Beale, J.T., Layton, A.T., 2009. A velocity decomposition approach for moving interfaces in viscous fluids. J. Comput. Phys. 228, 3358–3367.

Bihs, H., Kamath, A., Alagan Chella, M., Aggarwal, A., Arntsen, Ø.A., 2016. A new level set numerical wave tank with improved density interpolation for complex wave hydrodynamics. Comput. & Fluids 140, 191–208.

Chawla, A., Kirby, J.T., 1996. Wave Transformation over a Submerged Shoal. CACR Rep. No. 96-03, Ocean Engineering Laboratory University of Delaware, Newark, Delaware.

Chen, Y.L., Hsiao, S.C., 2016. Generation of 3d water waves using mass source wavemaker applied to Navier–Stokes model. Coast. Eng. 109, 76–95.

Chen, Q., Kirby, J.T., Dalrymple, R.A., Kennedy, A.B., Chawla, A., 2000. Boussinesq modeling of wave transformation, breaking, and runup. ii: 2d. J. Waterw. Port Coast. Ocean Eng. 126, 48–56.

Choi, Y.M., Bouscasse, B., Ducrozet, G., Seng, S., Ferrant, P., Kim, E.S., Kim, Y.J., 2023. An efficient methodology for the simulation of nonlinear irregular waves in computational fluid dynamics solvers based on the high order spectral method with an application with openfoam. Int. J. Nav. Archit. Ocean Eng. 15, 100510.

Cui, Z., Yang, Z., Jiang, H.Z., Huang, W.X., Shen, L., 2018. A sharp-interface immersed boundary method for simulating incompressible flows with arbitrarily deforming smooth boundaries. Int. J. Comput. Methods 15, 1750080.

Dommermuth, D.G., 1993. The laminar interactions of a pair of vortex tubes with a free surface. J. Fluid Mech. 246, 91–115.

Edmund, D.O., Maki, K.J., Beck, R.F., 2013. A velocity-decomposition formulation for the incompressible Navier–Stokes equations. Comput. Mech. 52, 669–680.

Engsig-Karup, A.P., Hesthaven, J.S., Bingham, H.B., Madsen, P.A., 2006. Nodal dg-fem solution of high-order boussinesq-type equations. J. Eng. Math. 56, 351–370.

Ferrant, P., Gentaz, L., Alessandrini, B., Le Touzé, D., de Nantes, Ecole Centrale, 2003. A potential/ranse approach for regular water wave diffraction about 2-d structures. Ship Technol. Res. 50, 165–171.

Gobbi, M.F., Kirby, J.T., 1999. Wave evolution over submerged sills: Tests of a high-order boussinesq model. Coast. Eng. 37, 57–96.

Higuera, P., Losada, I.J., Lara, J.L., 2015. Three-dimensional numerical wave generation with moving boundaries. Coast. Eng. 101, 35–47.

Hirt, C.W., Nichols, B.D., 1981. Volume of fluid (vof) method for the dynamics of free boundaries. J. Comput. Phys. 39, 201–225.

Hunt, J., Wray, A., Moin, P., 1988. Eddies, streams, and convergence zones in turbulent flows. In: Studying Turbulence using Numerical Simulation Databases-1. pp. 193–208.

Iafrati, A., 2009. Numerical study of the effects of the breaking intensity on wave breaking flows. J. Fluid Mech. 622, 371–411.

Islam, H., Mohapatra, S.C., Gadelho, J., Guedes Soares, C., 2019. Openfoam analysis of the wave radiation by a box-type floating structure. Ocean Eng. 193, 106532.

Jacobsen, N., 2011. A Full Hydro- and Morphodynamic Description of Breaker Bar Development (Ph.D. thesis).

Jacobsen, N.G., Fuhrman, D.R., Fredsøe, J., 2012. A wave generation toolbox for the open-source cfd library: Openfoam®: Wave generation toolbox. Internat. J. Numer. Methods Fluids 70, 1073–1088.

Kim, J., Moin, P., 1985. Application of a fractional-step method to incompressible Navier-Stokes equations. J. Comput. Phys. 59, 308–323.

Lee, J.I., Kim, Y.T., Cho, Y.S., 2013. Hydraulic experiments for wave transformation over a submerged elliptic shoal. J. Coast. Res. 291, 196–204.

Li, Z., Bouscasse, B., Ducrozet, G., Gentaz, L., Le Touzé, D., Ferrant, P., 2021. Spectral wave explicit navier-stokes equations for wave-structure interactions using two-phase computational fluid dynamics solvers. Ocean Eng. 221, 108513.

Li, Z., Deng, G., Queutey, P., Bouscasse, B., Ducrozet, G., Gentaz, L., Le Touzé, D., Ferrant, P., 2019. Comparison of wave modeling methods in cfd solvers for ocean engineering applications. Ocean Eng. 188, 106237.

Liu, X.D., Fedkiw, R.P., Kang, M., 2000. A boundary condition capturing method for Poisson's equation on irregular domains. J. Comput. Phys. 160, 151–178.

Lu, M., Yang, Z., He, G., 2023. An interface-resolved phase-change model based on velocity decomposition. J. Comput. Phys. 475, 111827.

Luquet, R., Alessandrini, B., Ferrant, P., Gentaz, L., 2003. Ranse analysis of 2D flow about a submerged body using explicit incident wave models. In: Numerical Towing Tank Symposium.

Luquet, R., Ducrozet, G., Gentaz, L., Ferrant, P., Alessandrini, B., 2007. Application of the swense method to seakeeping simulations in irregular waves. In: Proceedings of the 9th International Conference on Numerical Ship Hydrodynamics.

Luth, H.R., Klopman, G., Kitou, N., 1994. Kinematics of Waves Breaking Partially on an Offshore Bar; Ldv Measurements of Waves with and Without a Net Onshore Current. Report H-1573, Delft Hydraulics, p. 40.

Mirjalili, S., Jain, S., Dodd, M., 2017. Interface-capturing methods for two-phase flows: An overview and recent developments. Cent. Turbul. Res. Annu. Res. Brief 11, 7–135.

Mirjalili, S., Mani, A., Lele, S.K., Moin, P., 2019. A Novel Diffuse Interface Method for Two-Phase Flows and Application in Simulation of Micro-Bubble Entrainment (Ph.D. thesis). Stanford University, Stanford, California.

Mittal, A., Briley, W.R., Sreenivas, K., Taylor, L.K., 2017. A parabolic velocity-decomposition method for wind turbines. J. Comput. Phys. 330, 650–667.

Mohapatra, S.C., Islam, H., Guedes Soares, C., 2020. Boussinesq model and cfd simulations of non-linear wave diffraction by a floating vertical cylinder. J. Mar. Sci. Eng. 8 (575).

Mohapatra, S.C., Islam, H., Hallak, T.S., Soares, C.G., 2022. Solitary wave interaction with a floating pontoon based on boussinesq model and cfd-based simulations. J. Mar. Sci. Eng. 10, 1251.

Nguyen, V.T., Park, W.G., 2016. A free surface flow solver for complex three-dimensional water impact problems based on the VOF method. Internat. J. Numer. Methods Fluids 82, 3–34.

Nguyen, V.T., Park, W.G., 2018. Enhancement of Navier–Stokes solver based on an improved volume-of-fluid method for complex interfacial-flow simulations. Appl. Ocean Res. 72, 92–109.

Patel, J.K., Natarajan, G., 2015. A generic framework for design of interface capturing schemes for multi-fluid flows. Comput. & Fluids 106, 108–118.

Pathak, A., Jin, W., Raessi, M., 2023. A three-dimensional numerical scheme for modeling discontinuous pinning at sharp edges using the volume-of-fluid method. J. Comput. Phys. 479, 111986.

Paulsen, B.T., Bredmose, H., Bingham, H.B., Jacobsen, N.G., 2014. Forcing of a bottom-mounted circular cylinder by steep regular water waves at finite depth. J. Fluid Mech. 755, 1–34.

Popinet, S., 2009. An accurate adaptive solver for surface-tension-driven interfacial flows. J. Comput. Phys. 228, 5838–5866.

Rienecker, M.M., Fenton, J.D., 1981. A fourier approximation method for steady water waves. J. Fluid Mech. 104, 119–137.

Roenby, J., Bredmose, H., Jasak, H., 2016. A computational method for sharp interface advection. Royal Soc. Open Sci. 3, 160405.

Shin, Y., Sivasithamparam, N., Jung, T., Wang, H., Song, S., Park, S., Sim, J., 2017. Scour effet around suction bucket foundations and monopile in clay. In: Proceddings of the 8th International Conference. OSIG, Lodon, UK, pp. 276–283.

Sussman, M., Almgren, A.S., Bell, J.B., Colella, P., Howell, L.H., Welcome, M.L., 1999. An adaptive level set approach for incompressible two-phase flows. J. Comput. Phys. 148, 81–124.

Sussman, M., Puckett, E.G., 2000. A coupled level set and volume-of-fluid method for computing 3D and axisymmetric incompressible two-phase flows. J. Comput. Phys. 162, 301–337.

Tao, J., 2020. Numerical simulation of water waves. In: Springer Tracts in Civil Engineering. Springer, Singapore.

Vukčević, V., Jasak, H., Malenica, Š., 2016a. Decomposition model for naval hydrodynamic applications, part i: Computational method. Ocean Eng. 121, 37–46.

Vukčević, V., Jasak, H., Malenica, Š., 2016b. Decomposition model for naval hydrodynamic applications, part ii: Verification and validation. Ocean Eng. 121, 76–88.

Yang, Z., Lu, M., Wang, S., 2021. A robust solver for incompressible high-reynolds-number two-fluid flows with high density contrast. J. Comput. Phys. 441, 110474.

Zeng, Y., Bhalla, A.P.S., Shen, L., 2022a. A subcycling/non-subcycling time advancement scheme-based dlm immersed boundary method framework for solving single and multiphase fluid–structure interaction problems on dynamically adaptive grids. Comput. & Fluids 238, 105358.

Zeng, Y., Liu, H., Gao, Q., Almgren, A., Bhalla, A.P.S., Shen, L., 2023. A consistent adaptive level set framework for incompressible two-phase flows with high density ratios and high reynolds numbers. J. Comput. Phys. 478, 111971.

Zeng, Y., Xuan, A., Blaschke, J., Shen, L., 2022b. A parallel cell-centered adaptive level set framework for efficient simulation of two-phase flows with subcycling and non-subcycling. J. Comput. Phys. 448, 110740.

Zhao, B.B., Duan, W.Y., Ertekin, R.C., Hayatdavoodi, M., 2015a. High-level Green–Naghdi wave models for nonlinear wave transformation in three dimensions. J. Ocean Eng. Mar. Energy 1, 121–132.

Zhao, B., Duan, W., Webster, W., 2010. A note on three-dimensional green-naghdi theory. In: The 25th International Workshop on Water Waves and Floating Bodies. 25th IWWWFB.

Zhao, B.B., Ertekin, R.C., Duan, W.Y., 2015b. A comparative study of diffraction of shallow-water waves by high-level ign and gn equations. J. Comput. Phys. 283, 129–147.

Zhao, B., Zhang, T., Duan, W., Ertekin, R.C., Hayatdavoodi, M., 2019. Application of three-dimensional ign-2 equations to wave diffraction problems. J. Ocean Eng. Mar. Energy 5, 351–363.